EBSD measurement of strains in GaAs due to oxidation of buried AlGaAs layers ☆

R.R. Keller [a,*], A. Roshko [b], R.H. Geiss [a], K.A. Bertness [b], T.P. Quinn [a]

[a] *Materials Reliability Division, National Institute of Standards and Technology, 325 Broadway, Boulder, CO 80305, USA*
[b] *Optoelectronics Division, National Institute of Standards and Technology, 325 Broadway, Boulder, CO 80305, USA*

Abstract

We have characterized elastic strain fields associated with the wet-thermal oxidation of buried $Al_xGa_{1-x}As$ ($x \sim 0.98$) layers of thickness 80 nm, situated between GaAs layers of thickness 200 nm, on a GaAs substrate. The compressive strains accompanying oxidation can exceed 6% and may lead to interlayer delamination or fracture. Automated electron backscatter diffraction measurements were performed about individual oxide growth fronts on longitudinally cross-sectioned samples. We found that the elastic strain fields can be detected and mapped with a spatial resolution of better than 30 nm, using pattern sharpness quantification. Measured strain fields are elongated along the interfaces and extend approximately 1 μm around the growth front. We present efforts to quantify the spatial extent of these strain fields, as well as finite element simulations of the mechanics of oxide formation in this structure.
© 2004 Elsevier B.V. All rights reserved.

Keywords: EBSD; Oxidation; Strain

1. Introduction

We present the use of electron backscatter diffraction (EBSD) in a scanning electron microscope (SEM) for measuring elastically distorted regions of a multilayer compound semiconductor system, $Al_xGa_{1-x}As$/GaAs, containing a buried aluminum oxide layer. Such systems are central to the functionality of vertical cavity surface-emitting lasers (VCSELs), which present an attractive alternative to the limitations faced by conventional edge-emitting lasers. One benefit of the VCSEL architecture is the combination of both electron and photon confinement, afforded by the presence of an optical aperture, typically made of an amorphous aluminum oxide [1]. This aperture, however, is a potential source for serious reliability problems.

The aperture is formed by selective oxidation of the $Al_xGa_{1-x}As$ layer with the highest aluminum content [2]. Accompanying the conversion from $Al_xGa_{1-x}As$ to aluminum oxide is a severe volume

contraction. Although the observed oxide is an amorphous structure, an upper bound estimate of this contraction can be given by considering the case of crystalline γ-Al₂O₃ as compared to AlAs, which is a good approximation to $Al_xGa_{1-x}As$ with high aluminum content. The zincblende AlAs structure, with 4 aluminum atoms per unit cell, shows a volume per aluminum atom of 0.0448 nm^3. The defective spinel γ-Al₂O₃ structure [3] contains 21 aluminum atoms per unit cell, resulting in a volume per aluminum atom of 0.0235 nm^3. The resulting spacings between aluminum atoms in these materials differ by 20%, with that in alumina being smaller.

Cross-sectional TEM observations [4] from structures containing a buried amorphous aluminum oxide layer have indicated a linear contraction of approximately 7% upon transforming an AlAs layer to oxide. The discrepancy is largely due to the difference between crystalline and amorphous alumina. In VCSEL fabrication, thermal cycles subsequent to aperture formation can result in oxide/semiconductor delamination. In this paper, we demonstrate the application of automated EBSD for measuring distorted regions associated with the formation of buried oxide layers for optical apertures.

2. Experimental

Multilayer structures of $Al_xGa_{1-x}As/GaAs$ ($x \sim 0.98$) were grown by molecular beam epitaxy onto (0 0 1) GaAs substrates. We refer subsequently to the $Al_xGa_{1-x}As$ as AlGaAs for simplicity. Aluminum-containing layers were approximately 80 nm thick and the GaAs layers 200 nm thick. Wet thermal oxidation at 460 °C

was performed for 5 min along edges associated with channels etched into the top surface of the structure. This caused formation of alternating layers of aluminum oxide laterally into the multilayer stack. Typical oxidation lengths were in the range of tens of micrometers.

Electron backscatter diffraction measurements were made on freshly-cleaved specimens in a Schottky-emitting SEM, operated at 15 kV. To minimize issues such as specimen/stage drift, all scans were completed in 5 min or less. All data presented here is in its "raw" form, i.e., we used no data "clean-up" algorithms sometimes available in commercial EBSD software. Details addressing EBSD spatial resolution are presented later.

3. Results and discussion

3.1. Strain determination by EBSD: constant elastic strain

We begin with the simple case of a load applied along one axis of a cubic crystal. Bragg's law implies that the associated change in lattice spacing for that crystal direction will cause the scattering angle for the corresponding family of planes to vary inversely with the sense of the load, for constant electron energy. For example, a tensile load along a [1 0 0] direction would cause the (1 0 0) interplanar spacing to increase and the (1 0 0) Bragg angle to decrease. This would be detected in the EBSD pattern as a decrease in Kikuchi band width, as depicted schematically in Fig. 1. A multiaxial strain state would affect multiple Kikuchi bands in an analogous manner. Shear strains make analysis somewhat more complex, since both lattice spacings and lattice angles are expected to

$$W(\varepsilon = 0) = 2\theta_{hkl(0)} \qquad W(\varepsilon > 0) = 2\theta_{hkl(tens.)} < 2\theta_{hkl(0)}$$
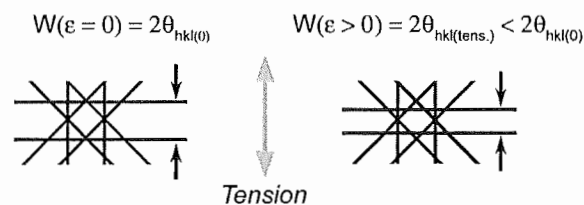

Tension

Fig. 1. Effect of tensile elastic strain on Kikuchi band width.

change. In that case, we expect changes in band widths as well as angles between bands. In principle a single diffraction pattern should contain information about many components of an elastic strain tensor. We note that research on extracting elastic strain states using the geometrically identical convergent-beam electron diffraction method [5] suggests that the process can be tedious.

Using these ideas, we performed a calibration using GaAs ($a_0 = 0.5653$ nm) and GaP ($a_0 = 0.5451$ nm), which have a lattice parameter mismatch of 3.6%. Intensity profiles across (4 4 0) Kikuchi bands revealed a difference of 3.4%, which compares favorably. Uncertainties in strain determination by EBSD within a uniform elastic field arise from several factors, including detector resolution, Kikuchi line curvature, and energy coherency of the incident electron beam. All of these factors limit the method to an uncertainty of approximately 0.2% strain, for relative strain measurement.

3.2. Strain determination by EBSD: elastic strain gradient

The discussion of uniform strain effects on Kikuchi band width suggests that if the electron beam were sampling a volume of material containing a non-uniform strain, then one should expect a non-uniform distribution of Bragg angles and therefore Kikuchi band widths. The distribution in Bragg angles would be manifest as an increase in the width of the *edge* of a Kikuchi band, as shown in Fig. 2. Effectively, the pattern loses "sharpness," sometimes referred to as image quality (*IQ*).
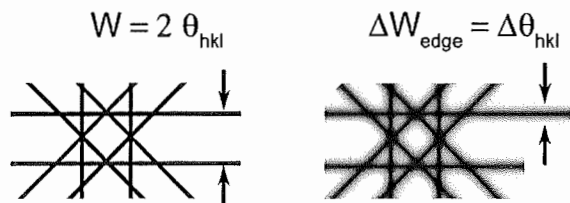

Fig. 2. Effect of elastic strain gradient on Kikuchi band width. The originally sharp line edge associated with a single d-spacing broadens as numerous interplanar spacings contribute to the band.

Concurrent with a change in pattern sharpness is a decrease in overall pattern contrast, which is a somewhat subtler effect. We refer to the dynamical electron diffraction discussion in [6] for quantitative details. For a constant number of electrons scattering out of a crystal in some unit of time, a perfect or uniformly strained crystal will exhibit a well-defined EBSD rocking curve (intensity profile across a Kikuchi band), with a distinct intensity maximum within the interior of the band, between the two Bragg scattering angles. The contrast across a Bragg angle for such a band depends upon the difference in backscattering efficiency between the most strongly excited Bloch wave on either side of the Bragg position and the inelastically scattered background signal. The set of Bloch waves in this case has the periodicity of the perfect or uniformly strained lattice. An elastic strain gradient across the sampling volume of the electron beam requires that what was initially a single set of periodic Bloch waves in the perfect crystal becomes a distribution of waves with amplitudes that depend upon position [7]. This requires that backscattering out of any one Bloch wave becomes much less efficient than that for the case of a perfect or uniformly strained crystal. The inelastically scattered background, on the other hand, should remain unaffected. This results in an overall decrease in contrast, of which we can take advantage.

Manufacturers of EBSD systems have relied upon a Hough transformation approach to automate the pattern indexing process. This method has resulted in the definition of a parameter that can be termed a pattern sharpness or *IQ* figure. For one such system, the *IQ* parameter is defined by:

$$IQ \equiv \sum_{hkl} (I_{max}), \tag{1}$$

where I_{max} is the maximum Hough peak intensity for plane (*hkl*). The summation is taken over several prominent peaks in the Hough space. We note also that:

$$I_{max}(\text{Hough}) \propto \sum (I_{pix}(\text{Kikuchi})), \tag{2}$$

where $I_{max}(\text{Hough})$ is the maximum intensity for one peak in the Hough space, and $I_{pix}(\text{Kikuchi})$ is a

pixel intensity for the corresponding Kikuchi band in the diffraction pattern, summed over all pixels in the band. So, *IQ* then is a direct measure of Kikuchi band intensities. If we assume that an elastic strain gradient is the primary reason for a decrease in pattern sharpness or *IQ*, then the *IQ* parameter is a direct measure of the severity of the gradient. Even for the same overall average strain in the sampling volume, a stronger gradient should show greater degradation of pattern sharpness than a weaker gradient. In other words, the *IQ* parameter as defined in Eq. (1) would decrease much more for the case of a strong strain gradient than a weaker one.

3.3. Distortion about a buried oxide layer

We performed an automated EBSD scan from a region in the vicinity of the growth front of an oxide layer, with the result shown in Fig. 3. The figure shows an *IQ* map at the top, with darker pixels indicating poorer quality. The middle image is the corresponding SEM image, showing the presence of the AlGaAs, GaAs, and oxide layers. Included in the figure are two diffraction patterns indicative of how the quality or sharpness changes with location within the structure. The dashed line shows roughly the location of a region of high elastic distortion near the oxide growth front; it appears from the darker *IQ* pixels nearer the front, that the elastic strain gradient is more severe there. Additional scans repeatedly show such a distortion, according to both multiple measurements from the same specimen, as well as measurements made on other oxide layers. In general, we observe that the distorted region is elongated in a direction parallel to the oxide layer, and it extends approximately 1–2 μm in either direction of the front. Note that the *IQ* map also shows sensitivity to the different materials in the structure. Namely, since AlGaAs has an average atomic number smaller than that of GaAs, it scatters less strongly, and results in weaker diffraction patterns than those of GaAs. The distortion region, however, is still visible in the AlGaAs layers.

To assess the validity of the EBSD-determined distortion region, we performed a two-dimensional, anisotropic elastic finite element analysis
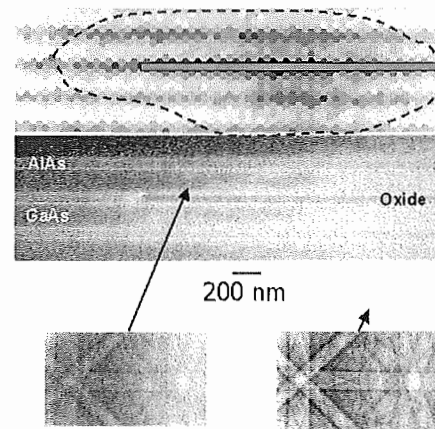

Fig. 3. *IQ* map (top) and corresponding SEM image (middle) from region near an oxide growth front. EBSD patterns show variation in pattern sharpness from locations near the front and in the substrate. Distortion region indicated approximately by dashed line in image quality map. The [0 0 1] direction is upward in the figure.

of this structure, assuming plane strain in order to estimate the strain state within the interior of the multilayer structure. We note, however, that our experimental results likely deviate from this assumption somewhat, since the specimen was cleaved in order to make measurements, and there will be some surface relaxation. For the model, we used elastic properties of γ-alumina for the buried oxide. We used tabulated properties for GaAs and AlAs [8], noting that these two materials are extremely similar elastically. Loading was accomplished through heating and assumption of appropriate coefficients of thermal expansion in order to achieve a 20% volume contraction in the oxide. As indicated earlier, the amorphous oxide exhibits a smaller contraction than this. However, we expect the materials to exhibit linear elastic behavior, so that the shape of the strain contours should remain the same, with magnitudes varying according to the applied strain.

Fig. 4 shows the calculated total strain fields in the *x*- and *y*-directions, associated with the presence of the buried oxide layer. In general, there is an elongated distortion field about the growth front, for each strain component. 1% contours extend approximately 1 μm away in each direction

from the end of the oxide. The shape of the distortion field for each component somewhat resembles the shape of the field as seen in the *IQ* map of Fig. 3, except for the lobes. We obtain even better shape agreement upon consideration of the von Mises equivalent strain field, which takes into account an averaged form of all strain components:

$$\varepsilon_{\text{vonMises}} = \frac{1}{\sqrt{2}} \left[\left(\varepsilon_x - \varepsilon_y \right)^2 + \left(\varepsilon_y - \varepsilon_z \right)^2 + \left(\varepsilon_z - \varepsilon_x \right)^2 \right.$$
$$\left. + 6 \left(\gamma_{xy}^2 + \gamma_{yz}^2 + \gamma_{xz}^2 \right) \right]^{1/2}. \qquad (3)$$

The *IQ* map is presented once again in Fig. 5, next to the von Mises field, which also shows the distortion. This representation more closely resembles the shape of the measured field seen in the *IQ* map. This suggests that the use of an *IQ* parameter for mapping strain fields is akin to displaying an averaged, total strain. Since the *IQ* parameter considers the effects of strain on many reflections simultaneously, it too represents an averaged strain. We are in the process of quantifying the *IQ* data to extract more detailed information about the nature of the elastic strain fields.

Use of the elastic properties of γ-alumina in the simulations is not entirely appropriate, as discussed earlier, and likely leads to different magnitudes of the strains, although the shape of the distortion field should be similar. We note also that the details of the geometry of the oxide front can strongly affect the distribution of strains and stresses. Careful TEM observations [9] show that the front can be rounded, with sharp corners. These features could skew the symmetry of the strain fields as determined by finite element simulation, as well as introduce stress concentrations that could increase the strains.
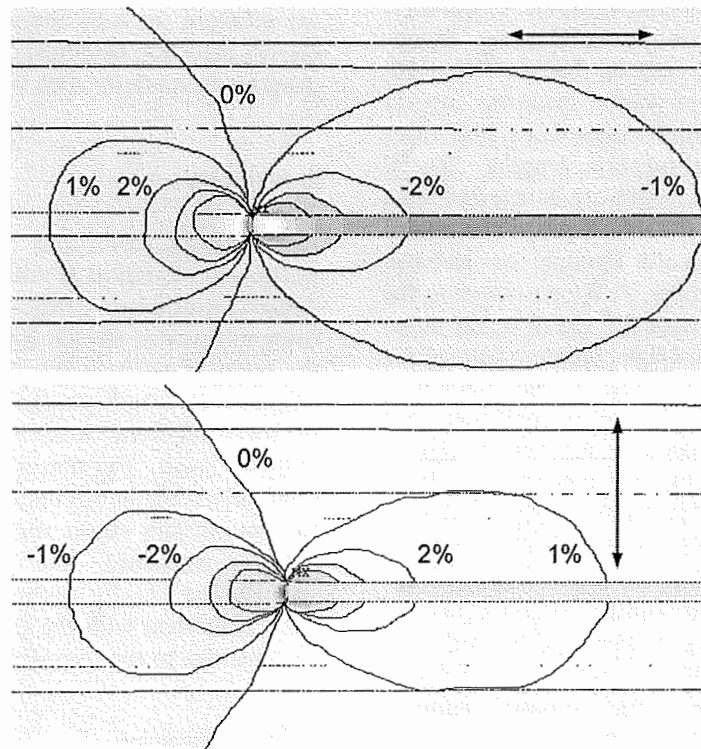

Fig. 4. Finite element simulations showing total strain fields in the *x*- and *y*-directions, associated with a 20% contraction of the buried oxide layer, located in the right portion of each plot. The strain components are indicated by the arrows, and contours are shown at 1% intervals.
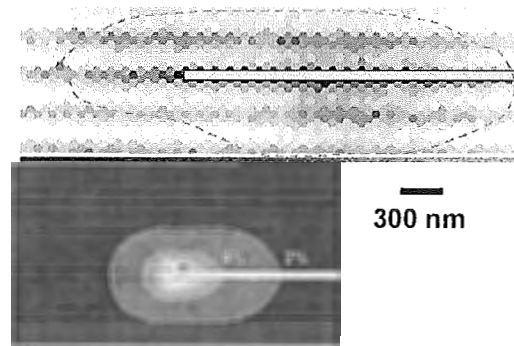
300 nm

Fig. 5. Distortion field about oxide tip, as revealed by dashed line in EBSD *IQ* map (top) and by finite element von Mises equivalent strain field plot (bottom). The map and the plot are shown at the same scale. The strain contours are shown at 2% intervals.

Fig. 6. High resolution EBSD *IQ* maps, showing more detailed detection of distortion field. Here, the redder pixels indicate a higher image quality parameter. Pixels within the AlAs and oxide layers have been thresholded into gray values for clarity.

3.4. EBSD spatial resolution considerations

We begin to estimate the spatial resolution of EBSD data by considering information volumes associated with the crystallographic orientation dependence of electron backscattering. Many-beam calculations of electron backscattered intensity as a function of crystal thickness suggest the majority of orientation-dependent signal arises from the top two absorption lengths, $2(\mu_0^{-1})$, within a crystal [6]; this length can be referred to as an information depth. μ_0 is the average absorption coefficient, which depends strongly on electron energy and atomic number, Z. We estimated μ_0 for GaAs ($\bar{Z} = 32$) using data for Ge ($Z = 32$) as an approximation [10]. Through considerations of the energy dependence of this factor, one can determine the variation in absorption coefficient and hence information depth as a function of microscope accelerating voltage. The result for $\bar{Z} = 32$ at 15 kV is a depth $2(\mu_0^{-1})$ of approximately 30 nm.

The data contained in the map of Figs. 3 and 5 was obtained by stepping the electron beam in increments of 35 nm, approximately the lateral size of the information volume. In analytically estimating the resolution of the method, we suggest that it is not simply the diameter of the sampling volume at each beam position that matters. That diameter may be considered an upper bound to a resolution estimate. More important is the minimum volume from which a change in the diffraction pattern can
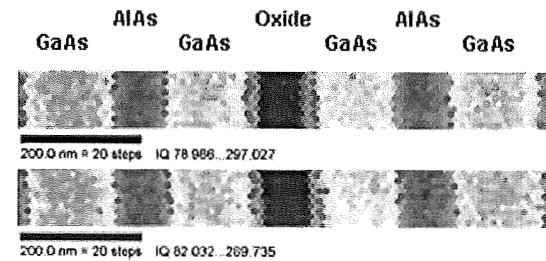
be detected. This volume is smaller than the information volume, and the corresponding lateral size represents the resolution of the method. Fig. 6 shows an *IQ* map with the beam stepped in 10 nm increments. The AlAs and GaAs layers have in this case become even more distinct than those observed at 35 nm. Note in particular the clarity of the edges of each of the layers. At this resolution, we measure an even smoother variation in the elastic distortion field near the oxide. Efforts are in progress to quantify such information.

4. Summary

The elastic distortions associated with the selective wet oxidation of AlGaAs layers in a GaAs/AlGaAs multilayer structure have been measured using automated EBSD. Results were presented in the form of pattern sharpness, or *IQ*, maps, the elements of which depend upon the severity of the localized elastic strain gradient sampled by the electron beam. The detected distortion fields are qualitatively similar to finite element predictions of the equilibrium strain state expected for such a complex structure. The von Mises equivalent strain most closely resembles the experimental data, consistent with the fact that EBSD patterns are sensitive to the overall strain state in a crystal.

Acknowledgements

References

[1] K.D. Choquette, K.M. Geib, C.I.H. Ashby, R.D. Twesten, O. Blum, H.Q. Hou, D.M. Follstaedt, B.E. Hammons, D. Mathes, R. Hull, IEEE J. Sel. Top. Quant. Electron. 3 (1997) 916–926.

[2] K.D. Choquette, K.M. Geib, H.C. Chui, B.E. Hammons, H.Q. Hou, T.J. Drummond, Appl. Phys. Lett. 69 (1996) 1385–1387.

[3] G. Gutiérrez, A. Taga, B. Johansson, Phys. Rev. B 65 (2001) 012101.

[4] R.D. Twesten, D.M. Follstaedt, K.D. Choquette, R.P. Schneider Jr., Appl. Phys. Lett. 69 (1996) 19–21.

[5] S. Krämer, J. Mayer, C. Witt, A. Weickenmeier, M. Rühle, Ultramicroscopy 81 (2000) 245–262.

[6] J.P. Spencer, C.J. Humphreys, P.B. Hirsch, Phil. Mag. 26 (1972) 193–213.

[7] P. Hirsch, A. Howie, R. Nicholson, E.W. Pashley, M.J. Whelan, Electron Microscopy of Thin Crystals, second ed., Robert Krieger Publishing, Malabar, FL, 1977, pp. 217–219.

[8] S. Adachi, Properties of Aluminum Gallium Arsenide, IEEE, London, 1993, pp. 23–24.

[9] R.D. Twesten, D.M. Follstaedt, K.D. Choquette, Proc. SPIE, in: K.D. Choquette, D.G. Deppe (Eds.), Vertical-Cavity Surface Emitting Lasers, vol. 3003, 1997, pp. 55–61.

[10] L. Reimer, Transmission Electron Microscopy, second ed., Springer, New York, 1989, pp. 302–303.